AGU ADVANCING EARTH AND SPACE SCIENCES

Geophysical Research Letters

RESEARCH LETTER
10.1029/2025GL117970

# Deep Argo Observations of Buoyancy Redistribution in the Atlantic Overturning

**Damien Desbruyères[1], Herlé Mercier[1], Gregory C. Johnson[2], Virginie Thierry[1], and Kjell Arne Mork[3]**

[1]Univ Brest, CNRS, Ifremer, IRD, Laboratoire d'Océanographie Physique et Spatiale (LOPS), IUEM, France, [2]Pacific Marine Environmental Laboratory, NOAA, Seattle, WA, USA, [3]Institute of Marine Research and Bjerknes Centre for Climate Research, Bergen, Norway

**Key Points:**

- Deep Argo reliably measures volume changes in the lower limb of the subpolar Atlantic Meridional Overturning Circulation
- Lower limb decadal and multidecadal volume trends are minimal, suggesting water mass transformation balances AMOC formation rate
- Interannual changes strongly affect the lower limb volume, so timescales matter when linking transformation rates and the AMOC

**Supporting Information:**

Supporting Information may be found in the online version of this article.

**Correspondence to:**

D. Desbruyères,
damien.desbruyeres@ifremer.fr

**Citation:**

Desbruyères, D., Mercier, H., Johnson, G. C., Thierry, V., & Mork, K. A. (2025). Deep Argo observations of buoyancy redistribution in the Atlantic overturning. *Geophysical Research Letters*, *52*, e2025GL117970. https://doi.org/10.1029/2025GL117970

Received 8 JUL 2025
Accepted 29 JUL 2025



**Abstract** The steady-state buoyancy budget of the Atlantic Meridional Overturning Circulation (AMOC) balances water mass transformation with meridional export. Using historical ocean data, Deep Argo observations, and atmospheric reanalysis, we assess the residual of this balance—water mass volume trends—and its role in the transformation budget of the Subpolar North Atlantic and Nordic Seas on interannual to bidecadal timescales. On long timescales, volume trends in deep convective seas can be large but the volume expansion or contraction of the upper and lower AMOC limbs remain minimal, suggesting that water mass transformation and AMOC intensity may be interchangeable. Conversely, interannual trends are larger across all regions and all density ranges. The volume of the AMOC limbs is significantly impacted so relationships with transformation rates can only be established when considering the timescales of the southward export of transformed water masses out of the subpolar domain.

**Plain Language Summary** The Atlantic Meridional Overturning Circulation (AMOC) is a system of ocean currents that relies on a balance between the light-to-dense transformation of water masses at high latitudes and their meridional flows from and towards low latitudes. Using novel ocean observations from Deep Argo floats, we analyze changes in the volume of these water masses on interannual to multidecadal timescales. Over long periods, the overall structure of AMOC remains stable despite large volume redistributions between deep water masses, suggesting a close link between water mass transformation and AMOC strength. However, on shorter timescales, volume redistributions between the AMOC limbs are more pronounced, making it difficult to directly infer AMOC intensity from transformation metrics.

## 1. Introduction

The global overturning circulation exerts a large control on the thermohaline structure of the ocean, ventilating its deep and abyssal layers with young upper waters and transporting them meridionally before they eventually return towards the surface through both diabatic (mixing-driven) and adiabatic (e.g., wind-driven Ekman pumping) processes. A key contributor to this deep ventilation is the along-stream density increase of upper waters and their localized deep convection in the Subpolar North Atlantic (SPNA) and in the Nordic Seas (e.g., Brambilla et al., 2008). The end product of this light-to-dense transformation is the so-called North Atlantic Deep Water (NADW), which feeds the lower limb of the Atlantic Meridional Overturning Circulation (AMOC) and carries relatively cold, oxygenated, and carbon-rich waters even to the Southern Ocean (e.g., Jackson et al., 2022; Mercier et al., 2024; Talley et al., 2011). Deep convection and AMOC intensity were for a long time considered causally linked. However, they represent distinct processes. Water mass transformation frameworks can illuminate whether and how variations in the production of dense waters influence the overturning (Walin, 1982). The NADW volume budget, that is, the balance among its formation rate, destruction rate, export rate, and local volume trend, is therefore a crucial indicator of climate dynamics (e.g., Desbruyères et al., 2019; Fu et al., 2024; M. S. Lozier, 2023; Mackay et al., 2020; Petit et al., 2020). The character of this balance is thought to be timescale-dependent. Changes in formation rates are likely to be balanced locally by changes in the volume of water masses on relatively short timescales (e.g., seasonal to interannual) and by large-scale export of water masses on longer timescales (e.g., decadal) (Buckley et al., 2023), although some modeling and observational analyses suggest rapid flushing (<1 year) of newly formed NADW by the boundary currents encircling the marginal seas of the SPNA (Feucher et al., 2019; Le Bras et al., 2020; Li et al., 2019). Assessing this hypothesis in models or observations remains challenging, due either to inherent biases in models or reanalyzes—especially in

the deep ocean—that can lead to unrealistically strong relationship between water mass transformation and meridional transport (i.e., overproduction of NADW and too weak interior recirculations) or due to the difficulty of measuring mixing-driven transformation rates (i.e., lack of widespread microstructure data) (Evans et al., 2023). However, unraveling how some components of the NADW budget have evolved over the past is becoming possible.

Until recently, the absence of basin-scale and continuous monitoring of water mass properties in deep and abyssal layers meant that analyses of NADW volume changes over the whole water column could only be done using ship-based hydrography data sets (e.g., Lherminier et al., 2010; Yashayaev, 2007). Those studies provide remarkable insights into the variability of NADW properties but inevitably suffer from sampling biases that limit their spatial and temporal representativeness (sparse repeats along nominal sections in summer). For instance, an analysis of abyssal volume trends in the Southern Ocean based on repeat hydrography sections revealed that the associated uncertainties often approach—or even exceed—the magnitude of the detected signals (Purkey & Johnson, 2012).

Now the technology routinely used since the early 2000s to measure the upper two km of the water column year-round—the global Argo array of profiling floats (Johnson et al., 2021; A. P. S. Wong et al., 2020)—is being extended to the seabed to fill in this gap. Its added value in supplementing repeat hydrography is already evident (Zilberman et al., 2023). For example, Deep Argo data have enabled more precise estimates of Antarctic Bottom Water warming trends (Johnson, 2022; Johnson et al., 2020) and revealed shorter-term changes, such as recent warming in the Southwest Pacific Basin (Johnson et al., 2019) or a reversal in Lower NADW temperatures in the mid-2010s (Desbruyères et al., 2022). This Deep-Argo array is particularly dense and homogeneous in the SPNA and Nordic Seas (Desbruyères et al., 2022; Petit et al., 2022; Racapé et al., 2019), which allows us to perform a comprehensive comparison of current NADW volume with historical climatology down to the seabed, and hence to assess imbalances between transformation rates and export rates during recent years and decades. Specifically, the strength of the regional Deep Argo array is to enable a first *full-depth* and *basin-scale* analysis of NADW volume changes with unprecedented low levels of uncertainty.

## 2. Data and Methods

The volume and buoyancy budget of a layer below an isopycnal surface $\sigma$—the so-called *Walin* framework (Walin, 1982)—is given by:

$$\partial_t V(\phi,\sigma) = F(\phi,\sigma) + M(\phi,\sigma) - \psi(\phi,\sigma) \quad (1)$$

which describes the balance of the surface-forced transformation $F$, the mixing-driven transformation $M$, the meridional export $\psi$, and the local rate of change of volume $\partial_t V$ (e.g., Buckley et al., 2023). Here, we seek to provide robust time-mean full-depth estimates of observed $\partial_t V$ on bidecadal, decadal, and interannual timescales. To do so, the height of evenly spaced $\sigma_1$ surfaces (resolution 0.01 kg m$^{-3}$) above the bottom—noted $h$ thereafter—is computed for a 2014–2023 collection of full-depth profiles of conservative temperature and absolute salinity, and using the maximum between the ETOPOv1 bathymetry and the deepest profile measurement as the bottom depth. The same is done with collocated profiles derived from $\frac{1}{4}^{\circ}$ World Ocean Atlas 2023 (WOA) decadal averages before computing the anomalies $h'$ (Johnson et al., 2019). The analysis is presented for a domain encompassing the SPNA (defined here to the north of 42°N and south of the Greenland-Iceland-Scotland sills and Davis Strait) and the Nordic Seas (NS hereafter), with the former further split into a western and an eastern subdomain (NWA and NEA hereafter) see insert in Figure 1b. The NWA and NEA are delimited here by the crest of the mid-Atlantic Ridge, which forms a natural boundary between relatively young and old NADW vintages (Rhein et al., 2015). This split is particularly relevant for the upper component of NADW formed within the northwestern SPNA, which often dominates NADW volume trends, as will be seen.

Our 2014–2023 data set is derived from a combination of full-depth Deep Argo and shipboard CTD profiles. The Deep Argo database consists of 4,820 profiles from an array of 66 Deep-Arvor 4,000 floats (Le Reste et al., 2016) deployed since 2014 (Figure 1). The nominal cycle duration of Deep Argo floats is 10 days. The nominal vertical resolution of Deep Argo profiles is platform-dependent but typically ranges between 1 and 2 db in the surface layer, 5–7 db in the intermediate layer, and 7–10 db in the deep layer. This array has been growing most in recent years, with a median date for all profiles in September 2021 and median dates of first and last float cycles in

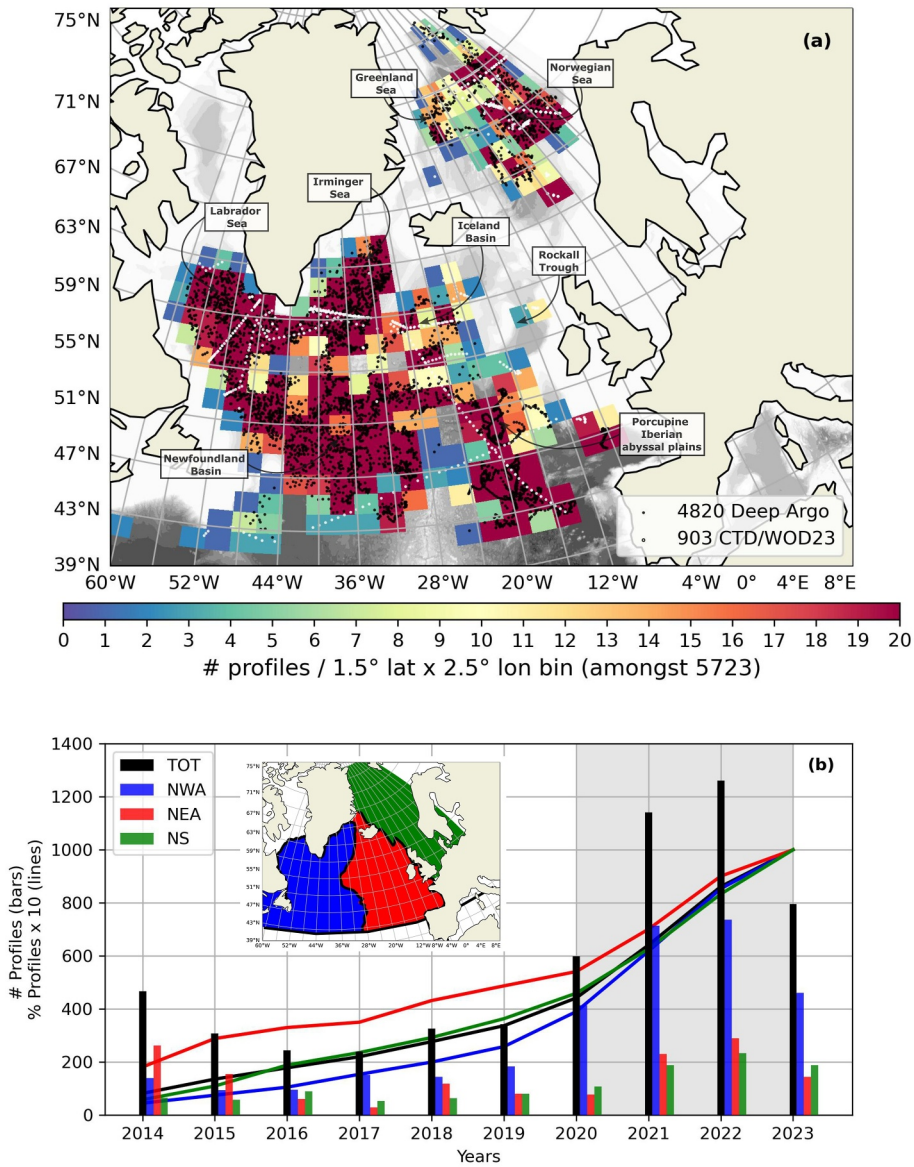


**Figure 1.** (a) Number of Deep-Argo profiles within 1.5° lat. × 2.5° long. grid cells. Location of the 5,723 profiles used in the analysis are shown with black and white dots for Deep Argo and shipboard CTD, respectively. The major basins mentionned in the text are labeled. (b) Time distribution of the Deep Argo profiles used in the analysis for SPNA (black), NWA (blue), NEA (red) and NS (green). Bars indicate the number of profiles per year and lines indicate the cumulative percentage of the database available each year. The densely sampled 4-year time-span 2020–2023 (gray shading) is used compute interannual volume changes (see Section 2). The insert shows the three subdomains analyzed: Northwest Atlantic (NWA; blue), Northeast Atlantic (NEA; red) and Nordic Seas (NS; green).

August 2020 and February 2023 respectively. Deep Argo deployments were repeatedly carried out within all major sub-basins and marginal seas of the SPNA and Nordic Seas, achieving a satisfactory homogeneous basin-scale sampling distribution in 2020. The interiors of the Labrador Sea, Irminger Sea, Norwegian Sea, Greenland Sea, and (northern) Newfoundland Basin all have profile concentration exceeding 20 per 1.5° lat. × 2.5° long. bin. Data coverage is as expected reduced but satisfactory in boundary regions, while data gaps exist in-between the Labrador and Irminger seas, in the interior of the Iceland basin, and in the Iberian abyssal plain. Data gaps in the eastern basins partly result from the use of only delayed-mode quality-controlled profiles (A. Wong et al., 2022) and will soon be filled following recent deployments. In the meantime, we further improve the spatial and temporal sampling coverage by complementing the Deep Argo database with 903 full-depth shipboard CTD

profiles from the World Ocean Database 2023, collected between 2014 and 2023. This results in a combined data set of 5,723 profiles for the time-span 2014–2023, and ensures that nearly all 1.5° lat × 2.5° lon bins—aligned with deep-ocean decorrelation length scales—are populated with data. It also enhances the sampling coverage for the earlier years, which were less sampled by Deep Argo floats.

The 2014–2023 Deep Argo/Shipboard CTD database is first compared against two decadal WOA averages that benefit from full-depth and high-quality hydrography data collected during the WOCE and subsequent GO-SHIP era: 1995–2004 (4,535 shipboard CTD profiles) and 2005–2014 (2,577 shipboard CTD profiles). The 1995–2004 and 2005–2014 decades captured contrasting upper NADW vintages in the SPNA: dense and homogeneous during 1995–2004 (following a period of relatively deep convection) and light and stratified during 2005–2014 (following a period of relatively shallow convection although punctuated by convective events in the latest years). The deep data distribution underlying the latest WOA average (2015–2022) is substantially reduced, with only 609 deep shipboard casts (see Figure S1 in Supporting Information S1). This sparseness motivates our decision to use our combined Deep Argo/Shipboard CTD data set (5,723 deep profiles) to characterize the 2014–2023 decadal state with improved spatial coverage. For each subdomain (NWA, NEA, NS), basin-mean profiles of $h'$ are obtained by evaluating a linear fit through 2014–2023 $h'$ values at the mid-point of the time-span (Jan 1st 2019; see Figure S2 in Supporting Information S1). This procedure affords more weight to be assigned to the earlier, less-sampled years, resulting in a more representative anomaly for the 2014–2023 period. Those $h'$ profiles are then converted into volume trends below $\sigma_1$ surfaces using the WOA-derived areas of $\sigma_1$ surfaces for each subdomain and the number of years from the mid-point of the WOA time-spans (Jan 1st 2000 for 1995–2004 and Jan 1st 2010 for 2005–2014) (e.g., Purkey & Johnson, 2012). At each density level, a 95% confidence interval for unweighted least squares regressions (Student's t-distribution) is provided using the residuals of the linear fit and a number of degrees of freedom computed as the number of distinct 1.5° lat. × 2.5° long. × 60-day bins containing at least one value of $h'$ (assuming decorrelation length and time scales of 160 km and 60 days, respectively following Purkey and Johnson (2010) and Johnson et al. (2015)). For the whole SPNA-NS domain, this number reaches ∼1700 circa $\sigma_1 = 32.4$ kg m$^{-3}$ and gradually decreases to 0 towards the deepest portion of the basins (at $\sigma_1 = 32.82$ kg m$^{-3}$, not shown). The large decrease in the number of degrees of freedom near the bottom causes an increase in the width of the confidence intervals.

Secondly, we follow Johnson et al. (2019) and estimate interannual volume trends during 2020–2023 for each subdomain by fitting linear functions versus time of $h'$ values at each density level regardless of profile locations and using the full 1955–2022 WOA23 average as a reference field (minor sensitivity to the reference field was confirmed using two additional climatologies: WOA23 climate normals for 1981–2010 and 1991–2020; not shown). This operation is done for six overlapping periods (2020–2021, 2021–2022, 2022–2023, 2020–2022, 2021–2023, 2020–2023), with standard errors and 95% confidence intervals derived as stated above. To focus on the magnitudes of the changes, rather than their signs, we analyze the root mean square and associated uncertainty of the six trend estimates. While the impact of potential aliasing of temporal and spatial variability in the climatology due to sparse and non-regular data distribution should not be neglected locally, it should largely average out in large-scale analysis such as the one presented here.

The magnitudes of $\partial_t V$ indicate whether an equilibrium between water mass transformation (surface-forced and mixing-driven) and export rates for any isopycnal layers (e.g., AMOC limbs or NADW components) holds for the latest bi-decadal (denoted $\partial_t V^{2018}_{2000}$ thereafter), decadal (denoted $\partial_t V^{2018}_{2010}$ thereafter), and interannual (denoted $\partial_t V^{2023}_{2020}$ thereafter) time-spans. Although the absence of diapycnal mixing estimates prevents a full closure of the water mass transformation budget, we evaluate the relative importance of $\partial_t V$ in front of $F$ by computing $|\frac{\partial_t V}{F}|$, where $F$ is computed monthly between 42°N and 80°N for each time span as:

$$F(\sigma) = \frac{1}{\Delta\sigma} \iint_{\phi>42N} \left[ \frac{\alpha}{C_p} Q + \beta \frac{S}{1-S} (E-P) \right] \Pi(\sigma) dx\, dy, \tag{2}$$

where $\alpha$ is the thermal expansion coefficient, $\beta$ is the haline contraction coefficient, $S$ is the surface salinity, $C_p$ is the specific heat, $Q$ is the heat flux into the ocean, and $E$ and $P$ are evaporation and precipitation, respectively (e.g., Grist et al., 2012; Marsh et al., 2005; Petit et al., 2020). $\Pi(\sigma'(x,y))$ selects the density outcrop and is given by

$$\Pi(\sigma(x,y)) = \begin{cases} 1, & \sigma - \frac{\Delta\sigma}{2} < \sigma \leq \sigma + \frac{\Delta\sigma}{2} \\ 0, & \text{elsewhere.} \end{cases}$$

Here, ocean surface variables ($\sigma, \alpha, \beta, S, C_p$) were obtained from the monthly EN4 4.2.2. Data set (Good et al., 2013) and atmospheric fluxes ($Q$, $E$, $P$) were obtained from the monthly ERA5 data set (Hersbach et al., 2020).

## 3. Results

Historical and modern shipboard hydrography surveys have allowed analysis of the characteristic and time-varying thermohaline properties of the water masses occupying the lower limb of the AMOC across key basins or passages of the SPNA-NS domain (e.g., Blindheim & Østerhus, 2005; de Jong & de Steur, 2016; Dickson et al., 2002; Lherminier et al., 2010; Petit et al., 2018; Piron et al., 2017; Yashayaev, 2007; Yashayaev & Loder, 2016). The key strength of the present combination of a dense Deep Argo array with shipboard CTD profiles lies in its unprecedented, nearly homogeneous consistent sampling of the full vertical and horizontal extents of the domain over a relatively short time window (in constrast approximately 64%, 63%, and 47% of the NWA, NEA, and NS volumes are not sampled by the core 0–2,000 m Argo array). Volumetric diagrams in the temperature-salinity space for the Deep Argo time-period (2014–2023) (Figure 2) capture the relatively fresh and warm core of Labrador Sea Water (LSW) formed in the northern NWA (Labrador and Irminger Seas) which reaches the NEA as a warmer and saltier water mass owing to mixing-driven isopycnal transformation. Below, both ISOW and DSOW, which respectively enter the SPNA in the NEA (Iceland-Scotland sills) and in the NWA (Denmark Strait) are notably lighter than their source, intermediate and deep water masses within the NS (some of which are too deep to spill across the sills). This relative lightness reflects the strong influence of entrainment-driven diapycnal mixing with upper mode waters and intermediate waters as the overflow plumes traverse the sills and cascade downward. As ISOW enters the NWA across the mid-Atlantic and Reykjanes ridges, it is further transformed through entrainment and mixing and develops into the voluminous NEADW, which is in turn further diluted by LSW and DSOW into a fresher product as it spreads westward and southward into the NWA. Volumetric diagrams using WOA averages for 1995–2004 and 2005–2014 (Figures S3 and S4 in Supporting Information S1, respectively) help to attribute specific volume changes to specific water masses based on their thermohaline properties instead of fixed density criteria.

The bidecadal anomaly (i.e., 2014–2023 minus 1995–2004) shows downwelling for almost all NADW isopycnal surfaces, likely reflecting AMOC-related multidecadal variability superimposed on long-term warming. The diapycnal structure of this downwelling reveals a large domain-mean sinking that reaches a first maximum value of $-150 \pm 31$ m at $\sigma_1 = 32.39$ kg m$^{-3}$ (Figure 3a, black line). This signal extends across the entire domain, but larger regional sinking amplitudes are observed in the NWA and NEA compared to the NS. Local anomalies can exceed 300 m in the interior of the Labrador and Irminger seas where deep convection is prominent, as well as in the Norwegian Sea and near the Mid-Atlantic Ridge (Figure 4a). In the NWA, negative anomalies are mostly confined to the intermediate density range ($\sigma_1 < \sim 32.47$ kg m$^{-3}$), whereas in the NEA, they remain substantial down to the seafloor. This pattern aligns with a striking contraction of ISOW source waters in the NS (up to $492 \pm 44$ m in the NSDW and GSDW isopycnal range) as well as with the general process in which ISOW entrains LSW signals as it cascades down the sills.

The streamfunction $\partial_t V_{2000}^{2018}$ shows that the dominant basin-mean contraction of the water column below $\sigma_1 = 32.39$ kg m$^{-3}$ and the expansion above it occurred at a rate of $2.20 \pm 0.14$ Sv (Figure 3b). This dense-to-light volume redistribution is equally partitioned between the NWA and the NEA but appears at slightly denser levels in the NWA, in line with the progressive density increases assocated with water mass transformation along the cyclonic gyre. Volumetric thermohaline diagrams (Figure 2 and Figure S3 in Supporting Information S1) reveal that this dominant signal is due to the formation (or expansion) of a relatively light LSW class (peaking at $\sigma_1 \sim 32.37$ kg m$^{-3}$ during 2014–2023; Figure 2) and the consumption of denser LSW and NEADW classes (peaking at $\sigma_1 \sim 32.42$ kg m$^{-3}$ and $\sigma_1 \sim 32.45$ kg m$^{-3}$ during 1995–2004, respectively; Figure S3 in Supporting Information S1). In the NS, the consumption of bottom waters reaches a maximum value of $1.01 \pm 0.09$ Sv at $\sigma_1 = 32.82$ kg m$^{-3}$.

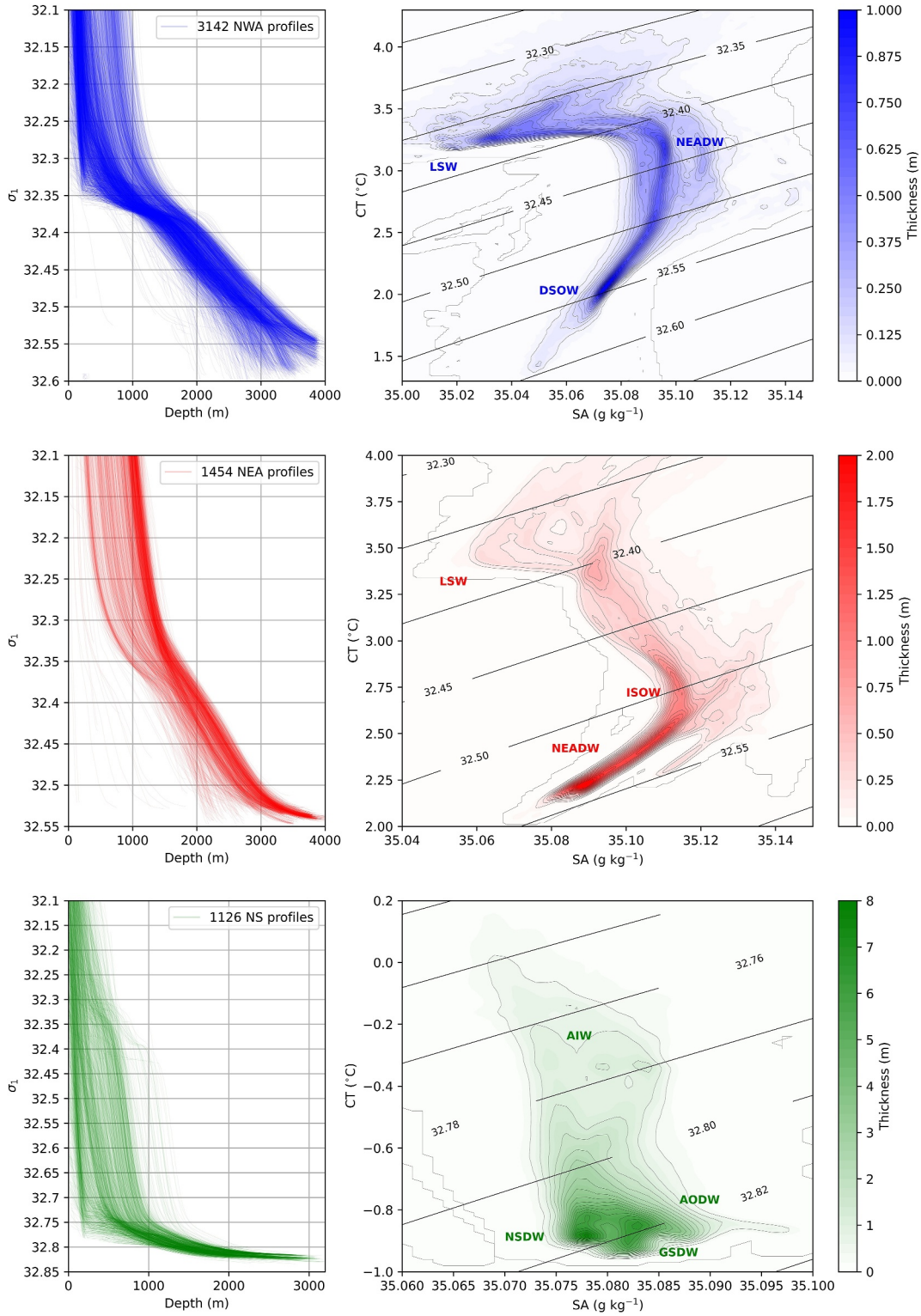


**Figure 2.** Depths (in m) of $\sigma_1$ isopycnal surfaces from the NWA (blue), NEA (red) and NS (green) subsets of Deep Argo and shipboard CTD profiles used in the present study and the corresponding conservative temperature-absolute salinity thickness diagrams. The thicknesses (in meters) of individual T-S bins were calculated for each profile with bin resolution 0.01°C × 0.001 g kg$^{-1}$, and then averaged across all profiles within each subdomain. Black contours shows $\sigma_1$ values. Acronyms are LSW (Labrador Sea Water), ISOW (Iceland Scotland Overflow Water), NEADW (North East Atlantic Deep Water), DSOW (Denmark Strait Overflow Water), AIW (Arctic Intermediate Water), NSDW (Norwegian Sea Deep Water), GSDW (Greenland Sea Deep Water), and AODW (Arctic Ocean Deep Water).

Last but not least, we find that $\partial_t V_{2000}^{2018}$ is small and insignificant at $\sigma_1 = 32.2$ kg m$^{-3}$ ($0.16 \pm 0.15$ Sv), which is near the typical density level of maximum SPNA overturning on observational overturning streamfunctions estimated at the southern exit of the SPNA (i.e., near the permanent pycnocline). This result suggests a balance between transformation and export rates on this bidecadal time-span for the whole AMOC lower limb. Formation due to surface buoyancy fluxes is largely balanced by consumption due to export and mixing down to $\sigma_1 \sim 32.35$ kg m$^{-3}$ (Figure 3). Below this density level and most particularly near the core of LSW range ($\sigma_1 \sim 32.4$ kg m$^{-3}$), $\partial_t V_{2000}^{2018}$ becomes an important contributor to the water mass transformation budget and accounts for at least 30% of the surface-forced transformation rates.

The decadal anomaly (i.e., 2014–2023 minus 2005–2014) in the depth of isopycnal surfaces shows the persistence of the dominant spatially homogeneous bidecadal anomaly, with a domain-mean sinking of $-74 \pm 28$ m at $\sigma_1 = 32.39$ kg m$^{-3}$ (Figure 3d) and a corresponding contraction below that isopycnal surface of $2.28 \pm 0.27$ Sv (Figure 3e). This magnitude aligns with the bidecadal estimate and suggests a temporally linear decrease in the volume of this particular layer. Likewise, the sinking of dense isopycnal surfaces in the NS is continued at a similar rate, with a domain-mean sinking of $-261 \pm 53$ m and a corresponding contraction of $1.01 \pm 0.21$ Sv at $\sigma_1 = 32.82$ kg m$^{-3}$. Most strikingly, the decadal anomaly additionally shows a large rising of isopycnal surfaces within the upper portion of the lower AMOC limb peaking at $\sigma_1 = 32.35$ kg m$^{-3}$ ($h' = 51 \pm 36$ m) (Figure 3d, black line). This large decadal signal is primarily found west of the mid-Atlantic ridge (NWA), with local upward displacements notably exceeding 500 m in the interior of the Labrador and Irminger Sea and as high as 250 m along the gyre western boundaries (Figure 4b). This new vintage of upper NADW has started to invade the Iceland Basin, while the farther regions (e.g., Iberian and Porcupine abyssal plains) are still occupied by the remnants of the earlier 1995–2004 vintage (negative $h'$). Overall, the decadal anomaly and its associated volume trend equate to an expansion of the 32.35 kg m$^{-3}$ $< \sigma_1 <$ 32.4 kg m$^{-3}$ density class of $3.9 \pm 0.65$ Sv, which is balanced by a contraction below $\sigma_1 = 32.39$ kg m$^{-3}$ and above $\sigma_1 = 32.35$ kg m$^{-3}$. Therefore, it suggests an accelerated expansion of the relatively light LSW class since the mid-1990s, at the expense of both denser and lighter classes (this pattern is also evident from the shift of the characteristic LSW salinity minima towards $32.35 < \sigma_1 < 32.40$ kg m$^{-3}$ density class in Figure S3 in Supporting Information S1 and Figure 2).

Finally, similar to the bidecadal trend, $\partial_t V_{2010}^{2018}$ remains small near the density level of maximum overturning ($0.07 \pm 0.31$ Sv at $\sigma_1 = 32.2$ kg m$^{-3}$), indicating a direct balance between transformation and export rates for the entire lower limb of the AMOC during this decadal time span (Figure 3f). However, the density level at which this balance breaks down decreases, with the ratio $|\frac{\partial_t V}{F}|$ now exceeding 30% below $\sigma_1 = 32.3$ kg m$^{-3}$.

Focusing on the amplitudes of the interannual changes, rather than the details, the RMS of interannual anomalies in the depth of isopycnal surfaces during 2020–2023 (Figure 3g) typically ranges between 25 and 125 m (large peaks exceeding 200 m at the very bottom of the NWA and NEA likely result from a limited number of data points). Uncertainties are as expected larger than for the bidecadal and decadal cases but anomalies remain statistically significant (at the 95% level) over the whole water column. The associated RMS of volume trends below isopycnal surfaces $\partial_t V_{2020}^{2023}$ (Figure 3h) are relatively large (i.e., compared to bidecadal and decadal values) and span the entire vertical extent of the AMOC lower limb. Again, the most significant volume changes are found within the LSW density range in the NWA, with RMS values as high as $5.45 \pm 1.80$ Sv at $\sigma_1 = 32.35$ kg m$^{-3}$. At higher densities, typically below $\sigma_1 = 32.40$ kg m$^{-3}$, volume trends are dominated by the NEA and NS.

At all density levels, the magnitude of $\partial_t V_{2020}^{2023}$ represents a substantial fraction of, and in some cases approaches, the surface-forced transformation $F$ (Figure 3i). In particular, and unlike the bidecadal and decadal trends, the interannual volume trends of the entire AMOC lower limb are non-negligible and can exceed 30% of $F$ below the typical density level of maximum overturning ($3.02 \pm 1.86$ Sv at $\sigma_1 \sim 32.2$ kg m$^{-3}$). This result suggests that a direct equilibrium between transformation rates and the AMOC is unlikely to exist on yearly timescales.

## 4. Conclusion and Discussion

The strength of the AMOC across a given latitude (or a trans-basin section) is often associated with the rate at which the relatively warm and light waters of its upper limb are transformed into the relatively cold and dense waters of its lower limb. This formation-to-export relationship, which is relevant to all isopycnal layers or components of the NADW, can only hold when changes in the volume of those layers north of the given latitude remain minimal. It is therefore likely to depend on the timescale of variability, specifically whether this timescale

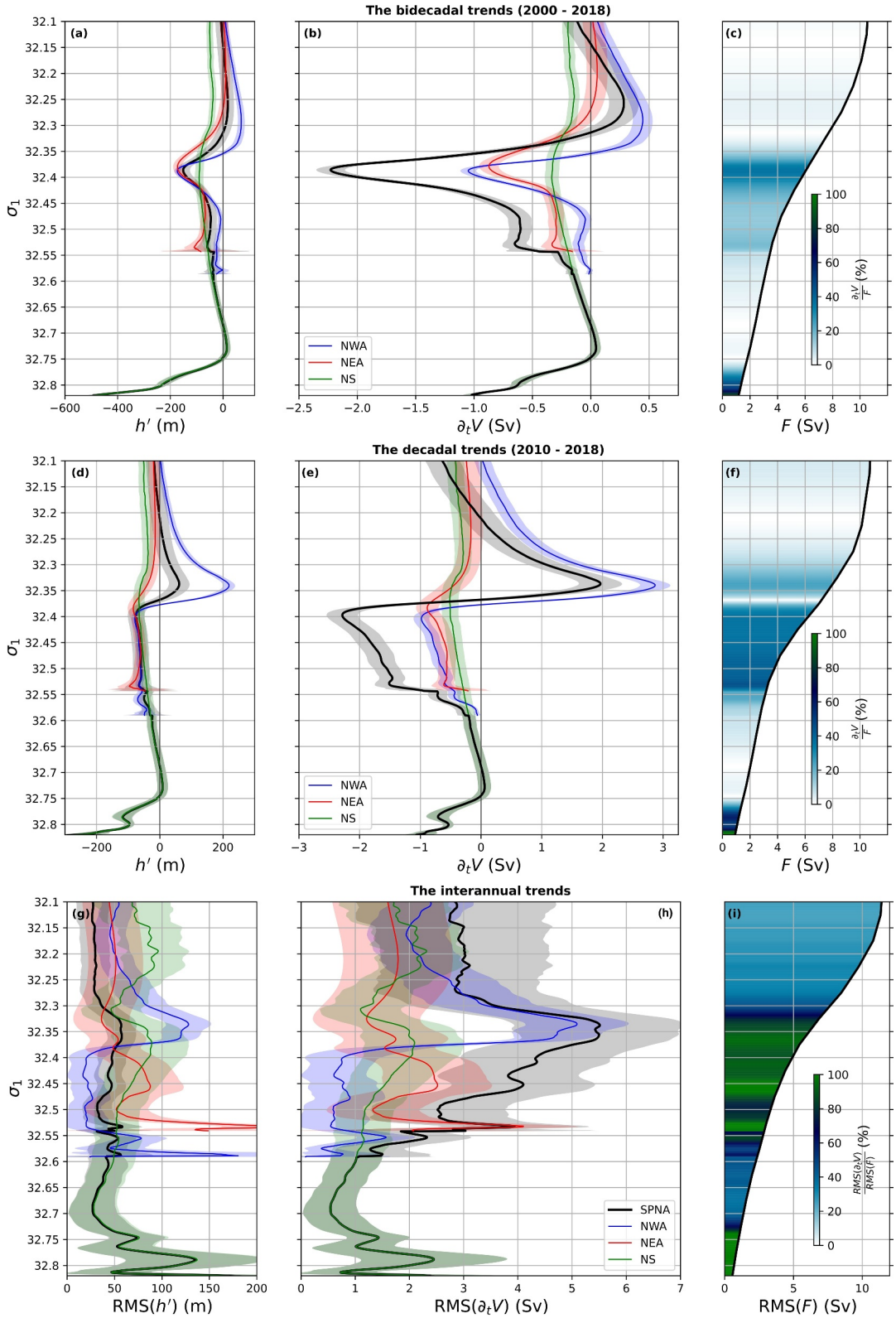


**Figure 3.**

is shorter or longer than the residence timescale of NADW in the SPNA. Here, we build on the availability of a novel *homogeneous* and *full-depth* Deep-Argo sampling of the SPNA and Nordic Seas (and hence on largely reduced uncertainties) supplemented by shipboard deep CTD data to assess this hypothesis from the density level of maximum overturning down to the seafloor, and during the latest bidecadal (2000–2018, 19 years), decadal (2010–2018, 9 years) and interannual (2020–2023) time-spans.

We find that the density level below which these transformation and export equilibrate decreases with timescale. On both bidecadal and decadal timescales, the basin-mean volume of the AMOC limbs (i.e., above and below the main pycnocline approximately) remains relatively constant, with linear volume trends negligible (and barely statistically significant) with respect to typical surface forcing and AMOC anomalies at the southern exit of the SPNA. In other words, anomalies in the volume of the AMOC lower limb, which are most likely caused by air-sea buoyancy fluxes, have sufficient time to propagate towards the southern exit of the domain (42°N herein) where they are ultimately "converted" into an anomalous streamfunction in the water mass transformation budget. Water mass transformation rates and AMOC magnitudes therefore appear to be interchangeable quantities on such timescales. This hypothesis aligns with the near-zero multidecadal volume trend of the AMOC limbs north of the OSNAP section in several reanalyzes (Fu et al., 2024). It also aligns with modeling analyses showing significant correlation between indices of surface-forced water mass transformation and AMOC intensity when the former is past-averaged over 10-yearlong windows (Grist et al., 2012). On shorter interannual timescales, volume trends of the AMOC limbs exceed the typical magnitude of observed AMOC variability (∼1.7 Sv for a 2-year lowpass filtered time series at 47°N in Wett et al. (2023)). Volume (or buoyancy) anomalies remain within the SPNA, preventing a direct balance between water mass transformation and the AMOC at the southern exit of the SPNA, so that the export of transformed water masses into boundary currents by eddies and out of the marginal seas and subpolar domain (e.g., Le Bras et al., 2020; M. Lozier et al., 2022) must be considered to develop meaningful proxies. This aligns with the strong 0-lag correlation between surface-forced transformation and AMOC volume trends in reanalyzes (Fu et al., 2024). It is also consistent with Desbruyères et al. (2019), who identified a 5-year lagged relationship between surface-forced transformation rates and AMOC variability at 45°N on multiyear timescales. Finally, it agrees with studies demonstrating a similar coupling mediated by the southward propagation of NADW anomalies along the boundary on such timescales, which subsequently influence horizontal circulation, ocean heat transport, and heat content (Chafik et al., 2023; Desbruyères et al., 2021; Kostov et al., 2021).

Across all timescales, individual NADW components can exchange volume locally at rates comparable to their distinct export along the boundary and representing a significant fraction of their surface-forced transformation. (e.g., Le Bras et al., 2020; Zantopp et al., 2017). On long time scales, such exchanges are generally more pronounced to the west of the MAR and for the LSW density range, and in the Nordic Seas in the density range of overflow source waters, reflecting the proximity of deep convection sites. The typical magnitude of the bidecadal and decadal volume trends reported herein agree with previous estimates based on shipboard hydrography (e.g., ∼2 Sv of LSW production over the 25-year period 1964–1972 to 1995–1997 in Yashayaev (2007)). The bidecadal and decadal trends reported here provide, for the first time on a basin-wide scale, a comprehensive quantification of the progressive depletion of the densest Labrador Sea Water vintage ever observed (formed in the early mid-1990s and commonly referred to as "classical" LSW) and the concurrent formation and eastward spreading of its lighter counterpart (known as "upper" LSW). The latter occurred at a faster rate since the mid-2000's, in line with a period of relatively strong atmospheric forcing and convective activity in the marginal seas of the SPNA, with a notable persisting positive phase of the North Atlantic Oscillation (NAO) during 2014–2023 (our Deep-Argo/Shipboard CTD time-span). Surface heat loss, convection depth, and (upper) NADW density all intensified during 2012–2018 before starting a recovery phase (still ongoing), which closed the second major cycle of intermediate water formation in the past four decades (Yashayaev, 2024). In the Nordic Seas, the bidecadal and decadal consumption of the densest components of NADW aligns with a sustained multi-decadal warming combined with surface freshening during the latest decade. This was likely due to increased inflow of less saline

**Figure 3.** Top line: (a) Basin-mean anomalous height of $\sigma_1$ surfaces $h'$ (units m) above the sea-floor (Deep-Argo minus WOA23) in the SPNA (black), NEA (red), NWA (blue) and NS (green) for the bidecadal 2000–2018 time-span (i.e., 2014–2023 minus 1995–2004). (b) The corresponding basin-mean rate of change of volume below $\sigma_1$ surfaces (in Sv). Shadings indicate the 95% confidence interval (see Section 2 for details). (c) The 2000–2018 mean surface-forced water mass transformation $F$ (see Equation 2) (black line), with coloring showing the quantity $\frac{\partial_t V}{F}$. (d, e, f) Same as panels (a, b, c) but for the decadal 2010–2018 time-span (i.e., 2014–2023 minus 2005–2014). (g, h, i) Same as panels (a, b, c) but for the RMS of six overlapping time-spans within 2020–2023 (see Section 2).

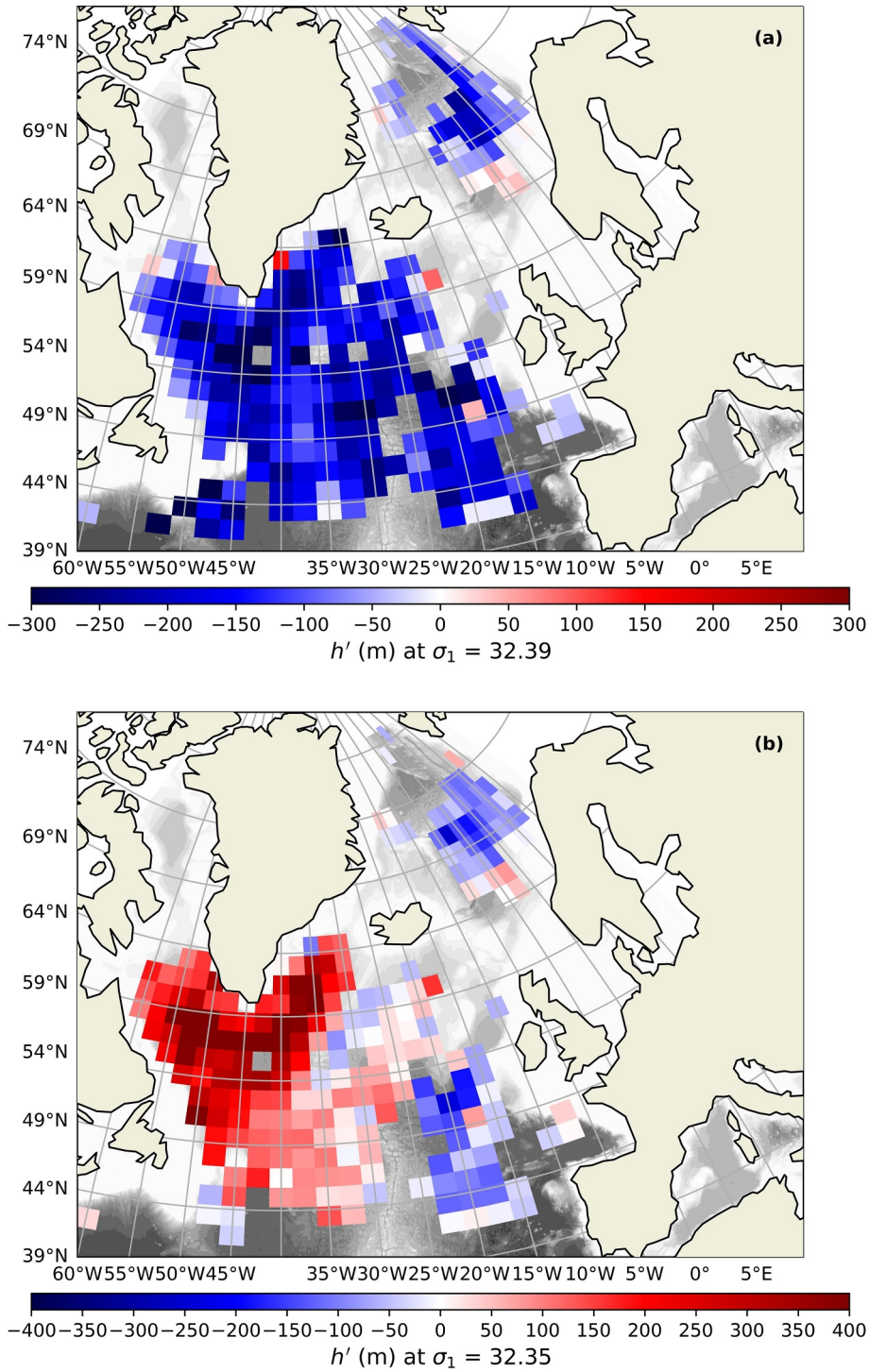


**Figure 4.** (a) Anomalous heights (in m) of $\sigma_1 = 32.39$ kg m$^{-3}$ computed from differences between Deep-Argo estimates and the collocated WOA23 1995–2004 climatology. (b) Anomalous heights of $\sigma_1 = 32.35$ kg m$^{-3}$ computed from differences between Deep-Argo estimates and the collocated WOA18 2005–2014 climatology. Anomaly profiles were averaged within a 1.5° latitude × 2.5° longitude horizontal grid.

Atlantic Water that has reduced convective mixing in recent years (Almeida et al., 2023; Mork et al., 2019; Strehl et al., 2024).

On shorter interannual timescales, the contribution of local volume trends to the water mass transformation budget increases across all basins and across the whole density range of the AMOC lower limb. As expected, volume trends within the density range occupied by upper NADW occur predominantly in the NWA where major convection sites are found, whereas the NEA and NS, which encompass major pathways of overflow-derived water masses (e.g., Zou et al., 2020), dominate at higher densities. Importantly, interannual volume trends within the whole NADW density range can typically be as high as their corresponding surface-forced transformation rates. Finally, interannual displacements of the density level of maximum overturning are as important in the NEA than in the NWA, aligning with previously reported patterns of surface-forced water mass transformation peaking in the Irminger, Iceland and Rockall basins (e.g., Buckley et al., 2023; Desbruyères et al., 2019; Kostov et al., 2021).

This analysis confirms the usefulness of ad hoc reconstructions of transformation rates from surface measurements of temperature and salinity and heat and salt fluxes when inferring the AMOC variability on timescales longer than a few years (Desbruyères et al., 2019; Fu et al., 2024; Petit et al., 2020). It also warns about the inappropriateness of this approach when inferring the export of distinct NADW components on all timescales, which require in situ measurements even on decadal and multi-decadal timescales (e.g., Zantopp et al., 2017). Finally, this analysis further demonstrates the key capabilities of Deep Argo floats to monitor the full water column year-round and over large spatial extents, and to derive key diagnostics on water mass property changes with unprecedented low level of uncertainties—up to three times lower than those derived from shipboard measurements alone (Figure S5 in Supporting Information S1). This capability is particularly valuable and timely for assessing the variability of deep ocean layers in climate models, which are increasingly used to predict the future behavior of the AMOC including the potential for abrupt slowdowns in the coming decades. Accelerating the implementation of the global Deep Argo array is therefore becoming an evident prerequisite not only to monitor the Earth Energy Imbalance precisely (von Schuckmann et al., 2023), but also to describe the climate-relevant dynamics (mean and variability) of ocean basins with energetic and deep-reaching vertical and diapycnal connections (see Zilberman et al. (2023) for a comprehensive review of Deep Argo achievements so far).

**Acknowledgments**
The authors thankfully acknowledge Cécile Cabanes and Anaïg Prigent for their hard work on the delayed-mode quality control of the Deep Argo profiles used in the present study. The authors also thank two anonymous reviewers for their constructive help. DD was funded under the French ANR project no. ANR-21-CE01-0011-01—CROSSROAD (Climatic Role of Subpolar-Subtropical exchanges: a Regional Observational Array off Newfoundland) and the Horizon Europe project 101059547—EPOC (Explaining and Predicting the Ocean Conveyor). GCJ's work on this study was supported by NOAA Global Ocean Monitoring and Observation Program and NOAA Research. PMEL Contribution Number 5685. VT gratefully acknowledges financial support by the following projects and grants: the Equipex + Argo-2030 project that received support from the French government within the framework of the "Investissements d'avenir" program integrated in France 2030 and managed by the Agence Nationale de la Recherche (ANR) under Grant Agreement ANR-21-ESRE-0019; the CPER Obsocean co-funded by the European Union, Région Bretagne, Département du Finistère, Brest Metropole and Ifremer. KAM acknowledges support by the Research Council of Norway (NorArgo2, #269753).

## Data Availability Statement

This study used ship-based CTD data from WOD 2023 (Garcia et al., 2024) downloaded from https://www.ncei.noaa.gov/products/world-ocean-database on 1 March 2025, and Deep Argo CTD data downloaded from an Argo Global Data Assembly Center on 28 February 2025 (Argo, 2000). These data were collected and made freely available by the International Argo Program and the national programs that contribute to it (https://argo.ucsd.edu, https://www.ocean-ops.org). The Argo Program is part of the Global Ocean Observing System. This study also uses ETOPO 2022 Bathymetry data (available at NOAA National Centers for Environmental Information (2022)).

## References

Almeida, L., Kolodziejczyk, N., & Lique, C. (2023). Large scale salinity anomaly has triggered the recent decline of winter convection in the Greenland Sea. *Geophysical Research Letters*, *50*(21), 1–10. https://doi.org/10.1029/2023GL104766

Argo. (2000). Argo float data and metadata from Global Data Assembly Centre (Argo GDAC). *SEANOE*. https://doi.org/10.17882/42182

Blindheim, J., & Østerhus, S. (2005). The nordic seas, main oceanographic features. In *Nord. Seas an integr. Perspect* (pp. 11–37). American Geophysical Union (AGU). https://doi.org/10.1029/158GM03

Brambilla, E., Talley, L. D., & Robbins, P. E. (2008). Subpolar mode water in the northeastern Atlantic: 2. Origin and transformation. *Journal of Geophysical Research: Oceans*, *113*(4), 1–16. https://doi.org/10.1029/2006JC004063

Buckley, M. W., Lozier, M. S., Desbruyères, D., & Evans, D. G. (2023). Buoyancy forcing and the subpolar Atlantic meridional overturning circulation. *Philosophical Transactions of the Royal Society A: Mathematical, Physical and Engineering Sciences*, *381*(2262), 20220181. https://doi.org/10.1098/rsta.2022.0181

Chafik, L., Penny Holliday, N., Bacon, S., Baker, J. A., Desbruyères, D., Frajka-Williams, E., & Jackson, L. C. (2023). Observed mechanisms activating the recent subpolar North Atlantic Warming since 2016. *Philosophical transactions. Series A, Mathematical, physical, and engineering sciences*, *381*(2262), 20220183. https://doi.org/10.1098/rsta.2022.0183

de Jong, M. F., & de Steur, L. (2016). Strong winter cooling over the Irminger Sea in winter 2014–2015, exceptional deep convection, and the emergence of anomalously low SST. *Geophysical Research Letters*, *43*(13), 7106–7113. https://doi.org/10.1002/2016GL069596

Desbruyères, D., Chafik, L., & Maze, G. (2021). A shift in the ocean circulation has warmed the subpolar North Atlantic Ocean since 2016. *Communications Earth & Environment*, *2*(1), 48. https://doi.org/10.1038/s43247-021-00120-y

Desbruyères, D. G., Bravo, E. P., Thierry, V., Mercier, H., Lherminier, P., Cabanes, C., et al. (2022). Warming-to-Cooling reversal of overflow-derived water masses in the Irminger Sea during 2002–2021. *Geophysical Research Letters*, *49*(10), 1–10. https://doi.org/10.1029/2022GL098057

Desbruyères, D. G., Mercier, H., Maze, G., & Daniault, N. (2019). Surface predictor of overturning circulation and heat content change in the subpolar North Atlantic. *Ocean Science*, *15*(3), 809–817. https://doi.org/10.5194/os-15-809-2019

Dickson, B., Yashayaev, I., Meincke, J., Turrell, B., Dye, S., & Holfort, J. (2002). Rapid freshening of the deep North Atlantic Ocean over the past four decades. *Nature*, *416*(6883), 832–837. https://doi.org/10.1038/416832a

Evans, D. G., Holliday, N. P., Bacon, S., & Le Bras, I. (2023). Mixing and air-sea buoyancy fluxes set the time-mean overturning circulation in the subpolar North Atlantic and Nordic Seas. *Ocean Science*, *19*(3), 745–768. https://doi.org/10.5194/os-19-745-2023

Feucher, C., Garcia-Quintana, Y., Yashayaev, I., Hu, X., & Myers, P. G. (2019). Labrador sea water formation rate and its impact on the local meridional overturning circulation. *Journal of Geophysical Research: Oceans*, *124*(8), 5654–5670. https://doi.org/10.1029/2019JC015065

Fu, Y., Lozier, M. S., Majumder, S., & Petit, T. (2024). Water mass transformation and its relationship with the overturning circulation in the Eastern subpolar North Atlantic. *Journal of Geophysical Research: Oceans*, *129*(12), e2024JC021222. https://doi.org/10.1029/2024JC021222

Garcia, H. E., Boyer, T. P., Locarnini, R. A., Reagan, J. R., Mishonov, A. V., Baranova, O. K., et al. (2024). World Ocean Database 2023 user's manual. https://doi.org/10.25923/j8gq-ee82

Good, S. A., Martin, M. J., & Rayner, N. A. (2013). EN4: Quality controlled ocean temperature and salinity profiles and monthly objective analyses with uncertainty estimates. *Journal of Geophysical Research: Oceans*, *118*(12), 6704–6716. https://doi.org/10.1002/2013JC009067

Grist, J. P., Josey, S. A., & Marsh, R. (2012). Surface estimates of the Atlantic overturning in density space in an eddy-permitting ocean model. *Journal of Geophysical Research: Oceans*, *117*(6), 1–14. https://doi.org/10.1029/2011JC007752

Hersbach, H., Bell, B., Berrisford, P., Hirahara, S., Horányi, A., Muñoz-Sabater, J., et al. (2020). The ERA5 global reanalysis. *Quarterly Journal of the Royal Meteorological Society*, *146*(730), 1999–2049. https://doi.org/10.1002/qj.3803

Jackson, L. C., Biastoch, A., Buckley, M. W., Desbruyères, D. G., Frajka-Williams, E., Moat, B., & Robson, J. (2022). The evolution of the North Atlantic meridional overturning circulation since 1980. *Nature Reviews Earth & Environment*, *3*(4), 241–254. https://doi.org/10.1038/s43017-022-00263-2

Johnson, G. C. (2022). Antarctic bottom water warming and circulation slowdown in the Argentine Basin from analyses of deep Argo and historical shipboard temperature data. *Geophysical Research Letters*, *49*(18), 1–7. https://doi.org/10.1029/2022GL100526

Johnson, G. C., Cadot, C., Lyman, J. M., McTaggart, K. E., & Steffen, E. L. (2020). Antarctic bottom water warming in the Brazil Basin: 1990s through 2020, from WOCE to deep Argo. *Geophysical Research Letters*, *47*(18), e2020GL089191. https://doi.org/10.1029/2020GL089191

Johnson, G. C., Hosoda, S., Jayne, S. R., Oke, P. R., Riser, S. C., Roemmich, D., et al. (2021). Argo—Two decades: Global oceanography. *Revolutionized*, *1–25*.

Johnson, G. C., Lyman, J. M., & Purkey, S. G. (2015). Informing deep argo array design using Argo and full-depth hydrographic section data. *Journal of Atmospheric and Oceanic Technology*, *32*(11), 2187–2198. https://doi.org/10.1175/JTECH-D-15-0139.1

Johnson, G. C., Purkey, S. G., Zilberman, N. V., & Roemmich, D. (2019). Deep Argo quantifies bottom water warming rates in the Southwest Pacific Basin. *Geophysical Research Letters*, *46*(5), 2662–2669. https://doi.org/10.1029/2018GL081685

Kostov, Y., Johnson, H. L., Marshall, D. P., Heimbach, P., Forget, G., Holliday, N. P., et al. (2021). Distinct sources of interannual subtropical and subpolar Atlantic overturning variability. *Nature Geoscience*, *14*(7), 491–495. https://doi.org/10.1038/s41561-021-00759-4

Le Bras, I., Straneo, F., Holte, J., Jong, M. F., & Holliday, N. P. (2020). Rapid export of waters formed by convection near the Irminger Sea's western boundary. *Geophysical Research Letters*, *47*(3), e2019GL085989. https://doi.org/10.1029/2019gl085989

Le Reste, S., Dutreuil, V., Andr??, X., Thierry, V., Renaut, C., Le Traon, P. Y., & Maze, G. (2016). Deep-Arvor: A new profiling float to extend the Argo observations down to 4000-m depth. *Journal of Atmospheric and Oceanic Technology*, *33*(5), 1039–1055. https://doi.org/10.1175/JTECH-D-15-0214.1

Lherminier, P., Mercier, H., Huck, T., Gourcuff, C., Perez, F. F., Morin, P., et al. (2010). The Atlantic meridional overturning circulation and the subpolar gyre observed at the A25-OVIDE section in June 2002 and 2004. *Deep Sea Research Part I: Oceanographic Research Papers*, *57*(11), 1374–1391. https://doi.org/10.1016/j.dsr.2010.07.009

Li, F., Lozier, M. S., Danabasoglu, G., Holliday, N. P., Kwon, Y.-O., Romanou, A., et al. (2019). Local and downstream relationships between Labrador Sea water volume and North Atlantic meridional overturning circulation variability. *Journal of Climate*, *32*(13), 3883–3898. https://doi.org/10.1175/JCLI-D-18-0735.1

Lozier, M., Bower, A. S., Furey, H. H., Drouin, K. L., Xu, X., & Zou, S. (2022). Overflow water pathways in the North Atlantic. *Progress in Oceanography*, *208*, 102874. https://doi.org/10.1016/j.pocean.2022.102874

Lozier, M. S. (2023). Overturning in the subpolar North Atlantic: A review. *Philosophical transactions. Series A, Mathematical, physical, and engineering sciences*, *381*(2262), 20220191. https://doi.org/10.1098/rsta.2022.0191

Mackay, N., Wilson, C., Holliday, N. P., & Zika, J. D. (2020). The observation-based application of a regional thermohaline inverse method to diagnose the formation and transformation of water masses north of the OSNAP array from 2013 to 2015. *Journal of Physical Oceanography*, *50*(6), 1533–1555. https://doi.org/10.1175/JPO-D-19-0188.1

Marsh, R., Josey, S. A., Nurser, A. J. G., de Cuevas, B. A., & Coward, A. C. (2005). Water mass transformation in the North Atlantic over 1985–2002 simulated in an eddy-permitting model. *Ocean Science*, *1*, 127–144. https://doi.org/10.5194/osd-2-63-2005

Mercier, H., Desbruyères, D., Lherminier, P., Velo, A., Carracedo, L., Fontela, M., & Pérez, F. F. (2024). New insights into the eastern subpolar North Atlantic meridional overturning circulation from OVIDE. *Ocean Science*, *20*(3), 779–797. https://doi.org/10.5194/os-20-779-2024

Mork, K. A., Skagseth, Ø., & Søiland, H. (2019). Recent warming and freshening of the Norwegian Sea observed by Argo Data. *Journal of Climate*, *32*(12), 3695–3705. https://doi.org/10.1175/JCLI-D-18-0591.1

NOAA National Centers for Environmental Information. (2022). ETOPO 2022 15 arc-second global relief model [Dataset]. *NOAA National Centers for Environmental Information*. https://doi.org/10.25921/fd45-gt74

Petit, T., Lozier, M. S., Josey, S. A., & Cunningham, S. A. (2020). Atlantic deep water formation occurs primarily in the Iceland basin and irminger sea by local buoyancy forcing. *Geophysical Research Letters*, *47*(22), 1–9. https://doi.org/10.1029/2020GL091028

Petit, T., Mercier, H., & Thierry, V. (2018). First direct estimates of volume and water mass transports across the Reykjanes Ridge. *Journal of Geophysical Research: Oceans*, *123*(9), 6703–6719. https://doi.org/10.1029/2018JC013999

Petit, T., Thierry, V., & Mercier, H. (2022). Deep through-flow in the Bight Fracture Zone. *Ocean Science*, *18*(4), 1055–1071. https://doi.org/10.5194/os-18-1055-2022

Piron, A., Thierry, V., Mercier, H., & Caniaux, G. (2017). Gyre-scale deep convection in the subpolar North Atlantic Ocean during winter 2014?? 2015. *Geophysical Research Letters*, *44*(3), 1439–1447. https://doi.org/10.1002/2016GL071895

Purkey, S. G., & Johnson, G. C. (2010). Warming of global abyssal and deep Southern Ocean waters between the 1990s and 2000s: Contributions to global heat and sea level rise budgets. *Journal of Climate*, *23*(23), 6336–6351. https://doi.org/10.1175/2010JCLI3682.1

Purkey, S. G., & Johnson, G. C. (2012). Global contraction of Antarctic bottom water between the 1980s and 2000s. *Journal of Climate*, *25*(17), 5830–5844. https://doi.org/10.1175/JCLI-D-11-00612.1

Racapé, V., Thierry, V., Mercier, H., & Cabanes, C. (2019). ISOW spreading and mixing as revealed by Deep-Argo floats launched in the Charlie Gibbs Fracture Zone. *J. Journal of Geophysical Research: Oceans*, *124*(10), 6787–6808. https://doi.org/10.1029/2019JC015040

Rhein, M., Kieke, D., & Steinfeldt, R. (2015). Advection of north Atlantic deep water from the Labrador Sea to the southern hemisphere. *Journal of Geophysical Research*, *120*, 2471–2487. https://doi.org/10.1002/2014JC010605.Received

Strehl, A.-M., Våge, K., Smedsrud, L. H., & Barreyre, T. (2024). A 70-year perspective on water-mass transformation in the Greenland Sea: From thermobaric to thermal convection. *Progress in Oceanography*, *227*, 103304. Retrieved from https://www.sciencedirect.com/science/article/pii/S0079661124001101doi:10.1016/j.pocean.2024.103304

Talley, L. D., Pickard, G. L., Emery, W. J., & Swift, J. H. (2011). Chapter 9 - Atlantic Ocean. In L. D. Talley, G. L. Pickard, W. J. Emery, & J. H. B. T. D. P. O. S. E. Swift (Eds.), *Descriptive Physical Oceanography* (6th ed, pp. 245–301). Academic Press. https://doi.org/10.1016/B978-0-7506-4552-2.10009-5

von Schuckmann, K., Minière, A., Gues, F., Cuesta-Valero, F. J., Kirchengast, G., Adusumilli, S., et al. (2023). Heat stored in the Earth system 1960–2020: Where does the energy go? *Earth System Science Data*, *15*(4), 1675–1709. https://doi.org/10.5194/essd-15-1675-2023

Walin, G. (1982). On the relation between sea-surface heat flow and thermal circulation in the ocean. *Tellus*, *34*(2), 187–195. https://doi.org/10.3402/tellusa.v34i2.10801

Wett, S., Rhein, M., Kieke, D., Mertens, C., & Moritz, M. (2023). Meridional connectivity of a 25-Year observational AMOC record at 47°N. *Geophysical Research Letters*, *50*(16), e2023GL103284. https://doi.org/10.1029/2023GL103284

Wong, A., Keeley, R., Carval, T., & Argo Data Management Team (2022). Argo Quality Control Manual For CTD and Trajectory Data. (Tech. Rep. No. December).

Wong, A. P. S., Wijffels, S. E., Riser, S. C., Pouliquen, S., Hosoda, S., Roemmich, D., et al. (2020). Argo data 1999–2019: Two million temperature-salinity profiles and subsurface velocity observations from a global array of profiling floats. *Frontiers in Marine Science*, *7*(700). https://doi.org/10.3389/fmars.2020.00700

Yashayaev, I. (2007). Hydrographic changes in the Labrador Sea, 1960-2005. *Progress in Oceanography*, *73*(3–4), 242–276. https://doi.org/10.1016/j.pocean.2007.04.015

Yashayaev, I. (2024). Intensification and shutdown of deep convection in the Labrador Sea were caused by changes in atmospheric and freshwater dynamics. *Communications Earth & Environment*, *5*(1), 156. https://doi.org/10.1038/s43247-024-01296-9

Yashayaev, I., & Loder, J. W. (2016). Recurrent replenishment of Labrador Sea Water and associated decadal-scale variability. *Journal of Geophysical Research: Oceans*, *121*(11), 8095–8114. https://doi.org/10.1002/2016JC012046

Zantopp, R., Fischer, J., Visbeck, M., & Karstensen, J. (2017). From interannual to decadal: 17 years of boundary current transports at the exit of the Labrador Sea. *Journal of Geophysical Research: Oceans*, 1–25. https://doi.org/10.1002/2016JC012271.Received

Zilberman, N. V., Thierry, V., King, B., Alford, M., André, X., Balem, K., et al. (2023). Observing the full ocean volume using Deep Argo floats. *Frontiers in Marine Science*, *10*, 1–12. https://doi.org/10.3389/fmars.2023.1287867

Zou, S., Bower, A., Furey, H., Susan Lozier, M., & Xu, X. (2020). Redrawing the IcelandScotland overflow water pathways in the North Atlantic. *Nature Communications*, *11*(1), 1890. https://doi.org/10.1038/s41467-020-15513-4